Optical Diagnostics of Spanwise-Uniform Flows

John Sontag* and Stanislav Gordeyev†
University of Notre Dame, Notre Dame, Indiana 46556

https://doi.org/10.2514/1.J061692

Aerooptical aberrations along the spanwise direction of a canonical subsonic turbulent boundary layer were measured and studied nonintrusively using a Shack–Hartmann wave front sensor. It was demonstrated that in this case some important fluidic statistics in the wall-normal direction, like the mean velocity profiles, the local skin friction, and the spanwise integral scales, can be directly extracted from aerooptical aberrations. To avoid various spectral contamination in optical data at low frequencies, a model function for the deflection angle autospectral density at low frequencies was proposed. The spectral cross-correlation method and the dispersion method were used to extract the local convective velocities, and the dispersion analysis was demonstrated to be most accurate in computing the velocities. It was shown that it is possible to reconstruct the spectra above the Nyquist frequencies through the newly proposed stacking method. Convective velocities in the log region of the turbulent boundary layer were found to agree well with the direct measurements using a single hot wire. From the convective velocities, the local wall shear stress was nonintrusively extracted, using the Clauser method. Using corrected deflection angle spectra and the convective velocity, the local values of aerooptical aberrations were reconstructed. Finally, using the strong Reynold's analogy, a wall-normal profile of the spanwise density correlation length was estimated and shown to be in good qualitative agreement with velocity-based spanwise length scales observed in the literature.

Nomenclature

A	=	proportionality constant
B	=	log/law constant
C_f	=	skin friction
cov	=	covariance matrix
E	=	two-point correlation
f	=	frequency, Hz
F	=	lens focal length, mm
fsamp	=	sampling frequency, Hz
K_{GD}	=	Gladstone–Dale constant, m^3/kg
k	=	wave number, 1/m
L	=	propagation length, m
M	=	Mach number
Mag	=	optical magnification rate
n	=	index of refraction
OPD	=	optical path difference, m
OPL	=	optical path length, m
P	=	pressure, Pa
R	=	two-point correlation
Re	=	Reynolds number
r	=	recovery constant
S	=	power spectral density
St_δ	=	Strouhal number, equal to $f\delta/U_\infty$
s	=	generic propagation direction, m
T	=	Fourier transform block time, s
t	=	time, s
U	=	mean velocity, m/s
u	=	velocity, m/s
W	=	wave front, m
x	=	streamwise direction, m
y	=	wall-normal direction, m
z	=	spanwise direction, m
α	=	linking equation constant
β	=	Clauser pressure gradient
Γ	=	dispersion parameter
γ	=	ratio of specific heats
Δ	=	finite change in variable
δ	=	boundary-layer thickness, mm
∂	=	partial derivative
θ	=	deflection angle, rad
κ	=	log/law constant
Λ	=	integral correlation length, m
ν	=	kinematic viscosity, m^2/s
ρ	=	density, kg/m^3
τ	=	wall shear stress, Pa

Subscripts

C	=	convective
rms	=	root mean square
S	=	stationary
w	=	wall quantity
ρ	=	density
ρ, z	=	density, in spanwise direction
τ	=	friction quantity
∞	=	freestream quantity

Superscripts

$+$	=	friction quantity
$\bar{(\cdot)}$	=	mean quantity
$'$	=	fluctuating quantity
$\widehat{}$	=	Fourier transform
$*$	=	complex conjugate

I. Introduction

THE field of optical measurement science has advanced dramatically since the dawn of the computer age. Our rapid advances in computer technology have helped to develop high-speed cameras with sampling frequencies on the order of megahertz. This has opened the door to some unique optical systems that are capable of keeping pace with the frontier of aerospace research at supersonic and hypersonic speeds. One such system is the Shack–Hartmann wave front sensor, which has been frequently used in the field of aerooptics, where the use of laser-based systems on airborne platforms is studied. Wave front sensors, in general, seek to measure some aspect of how light is optically distorted or aberrated. Light will travel in a straight line until it encounters an optically distorting region and bends.

Presented as Paper 2020-3235 at the AIAA Aviation Forum, Virtual Event, June 15–19, 2020; received 31 January 2022; revision received 29 April 2022; accepted for publication 27 May 2022; published online 21 June 2022.

*Graduate Student, Department of Aerospace and Mechanical Engineering, Student Member AIAA.

†Associate Professor, Department of Aerospace and Mechanical Engineering, Associate Fellow AIAA.

Measuring the degree to which the light is bent can tell us about these optical distortions and also gives us clues how to mitigate them [1,2]. Time series of the spatially resolved optical aberrations, when sampled with sufficient speed, allowed measuring the convective speeds of these aberrations. The convective speeds provide very useful information about the underlying flow structures, responsible for optical distortions, over a wide range of flow speeds [3–6].

Nonintrusive laser-based optical sensors, with a few exceptions, have traditionally been used in practical applications to understand the challenges associated with using laser-based communications and energy deposition systems on an airborne platform. These sensors have largely remained isolated from use as general optical measurement systems due to the specific usefulness in the field of aerooptics, unlike particle image velocimetry (PIV), for example. This is partly a result of the problem that all optical-based sensors face, namely, how to relate optical measurements to parameters that are more relevant to the wider aerospace scientific community, like local velocity or density. Therefore, if a wave front sensor is to be used as tool by the aerodynamic community, it is critical to establish this link between optical aberrations and more traditional fluid mechanics parameters.

An added difficulty of wave front sensors, with respect to usefulness as a general measurement tool, is their integral property. In other words, all of the small optical aberrations that a laser beam experiences as it travels through a fluid result in a cumulative or spatially integrated effect that is interpreted by the sensor as a bulk amount of optical distortion imposed on the traversed laser beam. As a result, any information about where the sources of optical distortion are located along the laser beam is typically lost. One exception is digital holography wave front sensors, where it is possible to recover some depth information [7]. Recently, several optical techniques were proposed to attempt measuring local fluidic properties nonintrusively. One technique, known as focused laser differential interferometry (FLDI) [8,9], uses a pair of convergent/divergent beams, polarized in orthogonal directions, to measure the density gradient near the focus location. The difference in optical path length between two beams will create interference when the beams are recombined on the photodetector, with the variation in intensity proportional to the density gradient. To perform simultaneous measurements of velocity and density gradients, two-point FLDI was developed, which involves using four convergent/divergent beams total, with a small separation near the focal point between the two pairs of beams in order to obtain a cross-correlation [10]. In addition to requiring a complex setup with several beams to measure convective velocity, another drawback of FLDI is that it may be affected by variations in ambient light intensity on the sensor. Another recently proposed technique, called a focused Malley probe [11], also uses two convergent/divergent laser beams, with focal points separated by a known distance in the streamwise direction. Global beam jitters of both beams are simultaneously measured using a high-speed camera, and the spectral cross-correlation analysis is implemented to extract the jitter spectra and the convective speed of the aerooptical structures near the focal points. It was demonstrated that the focused Malley probe is capable of correctly measuring the local jitter spectra and the related convective speed of the aerooptical structures near the focal points while suppressing aerooptical signal everywhere else via the aperture averaging effect [11].

Instead of attempting to develop another focused optical technique, the work described here presents a novel application of the traditional Shack–Hartmann wave front sensor to flows that are statistically uniform along the spanwise direction, which coincides with the path of the laser beam. Uniformity at all points means that the bulk value measured by the sensor is actually a statistically equal contribution from every point along the beam. In this case, it will be shown in the following section that aerooptical parameters are directly linked to local fluid mechanics parameters.

A. Relating Aerooptical Aberrations to Local Turbulence Quantities

The main aerooptical quantity of interest is the optical path length (OPL), which is defined as

$$\mathrm{OPL}(x,y,t)=\int_0^L n(x,y,z,t)\,\mathrm{d}z \tag{1}$$

where $n(x,y,z,t)$ is the index of refraction and the z axis is chosen to coincide with the direction of beam propagation. For the case of dry gases, the index of refraction is proportional to the local density via the Gladstone–Dale constant K_{GD} [2,12,13], $n(\boldsymbol{x},t)=1+K_{\mathrm{GD}}\rho(\boldsymbol{x},t)$. For air, K_{GD} is approximately $2.27\cdot 10^{-4}\ \mathrm{m}^3/\mathrm{kg}$ for visible wavelengths of light.

In practice, a spatial mean is removed from OPL to compute the optical path difference (OPD), $\mathrm{OPD}(x,y,t)=\mathrm{OPL}(x,y,t)-\langle \mathrm{OPL}(x,y,t)\rangle_{(x,y)}$. Here and everywhere in the following, the angled brackets denote the spatial averaging. OPD is directly related to the intensity distribution at a far field [14].

As discussed before, the integral relationship in Eq. (1) presents a difficulty in determining local values of $\rho(x,y,z,t)$. In an attempt to relate these quantities, Sutton [15] derived a theoretical formulation of an equation linking statistical properties of ρ and OPD, called the linking equation. Starting with the most general case where nothing is assumed about the flowfield, the linking equation takes the form

$$\mathrm{OPD}_{\mathrm{rms}}^2=K_{\mathrm{GD}}^2\int_0^L\int_0^L \mathrm{cov}_\rho(s,s')\,\mathrm{d}s'\,\mathrm{d}s \tag{2}$$

where $\mathrm{OPD}_{\mathrm{rms}}^2=\overline{\mathrm{OPD}^2(t)}$ is the local temporal variance of OPD at a fixed point on a plane, normal to the beam propagation; s and s' are positions along the direction of beam propagation; and L is the propagation length through the flowfield. The overbar here and later in this paper denotes time averaging. The linking equation in this form reveals that the variance in optical distortions of the wave front is related to the covariance of density fluctuations in the direction of propagation. The covariance function itself takes the form $\mathrm{cov}_\rho(s,s')=\overline{\rho'(s,t)\rho'(s',t)}$, where $\rho'(s)$ is the fluctuating density at location s. The most common assumption is that the flowfield is composed of homogeneous turbulence, and the covariance can be described by either exponential or Gaussian analytical forms [16] with a single parameter Λ_ρ, which represents a characteristic length of the density fluctuations. For these covariance functions, the linking equation becomes

$$\mathrm{OPD}_{\mathrm{rms}}^2=\alpha K_{\mathrm{GD}}^2\int_0^L \rho_{\mathrm{rms}}^2(s)\Lambda_\rho(s)\,\mathrm{d}s \tag{3}$$

with and α factor of 2 or $\sqrt{\pi}$ for the exponential and Gaussian distributions, respectively. This equation establishes the integral link between the statistics of the aberrated wave front, $\mathrm{OPD}_{\mathrm{rms}}$, and the local flow-related statistics, as ρ_{rms} and Λ_ρ. Equation (3) has been extensively validated both experimentally [3,4] and numerically [17,18] for laser beams traversing in the wall-normal direction and is widely used to estimate optical distortions from density statistics in spite of several assumptions, like homogeneous turbulence, that are not strictly valid.

In general, one needs to prescribe the spatial profiles of $\rho_{\mathrm{rms}}(y)$ and $\Lambda_\rho(y)$ along the laser beam to compute the overall level of aerooptical distortions $\mathrm{OPD}_{\mathrm{rms}}$. However, there are a number of flows that can be treated as spanwise uniform: boundary layers on a flat plate, two-dimensional shear layers, and cavity flows, to name some. If the laser beam is sent in the spanwise direction, denoted as the z direction, the linking equation can be significantly simplified. The essential change in assuming spanwise uniform flow is that the covariance function along the beam is no longer a function of absolute position z but only a relative position, $\Delta z=z-z'$. Therefore, returning to Eq. (2) and using the assumption of homogeneous turbulence along the spanwise direction reduces the linking equation from a covariance function to a two-point correlation function, resulting in the following equation for $\mathrm{OPD}_{\mathrm{rms}}$,

$$\mathrm{OPD}_{\mathrm{rms}}^2=K_{\mathrm{GD}}^2\int_0^L\int_{-z}^{L-z}\overline{\langle\rho'(z_0,t)\rho'(z_0+\Delta z,t)\rangle}\,\mathrm{d}\Delta z\,\mathrm{d}z$$

If we define the normalized two-point density correlation along the optical path $R_{\rho\rho}$ as

$$R_{\rho\rho}(\Delta z) = \frac{\overline{\langle \rho'(z,t)\rho'(z+\Delta z,t)\rangle}}{\rho^2_{\mathrm{rms}}}$$

and the spanwise density correlation length as

$$\Lambda_{\rho,z} = \frac{1}{2}\int_{-z}^{L-z} R_{\rho\rho}(\Delta z)\,\mathrm{d}\Delta z \tag{4}$$

then the linking equation becomes

$$\mathrm{OPD}^2_{\mathrm{rms}} = 2K^2_{\mathrm{GD}}\int_0^L \rho^2_{\mathrm{rms}}\Lambda_{\rho,z}\,\mathrm{d}z \tag{5}$$

The factor of 2 in Eq. (5) should not be confused with the multiplicative factor that results from assuming an exponential form of the covariance function in Eq. (3) but rather comes from the $1/2$ multiplier in the definition of $\Lambda_{\rho,z}$, Eq. (4). Because both the rms of density fluctuations and the density correlation length in the spanwise direction are constant along the integration path, Eq. (5) becomes

$$\mathrm{OPD}^2_{\mathrm{rms}}(x,y) = 2K^2_{\mathrm{GD}}\rho^2_{\mathrm{rms}}(x,y)\Lambda_{\rho,z}(x,y)L \tag{6}$$

Here, we explicitly recognized that all quantities can vary in the streamwise or x direction and the wall-normal, y direction. This equation provides a direct link between the local fluidic properties and overall optical distortions in the spanwise direction. Note that, unlike Sutton's linking Eq. (3), where the flow is assumed to be homogeneous, the only assumption used to derive Eq. (6) is that the flow is uniform in the spanwise direction.

The paper is organized as follows. Section II presents the experimental setup of the canonical boundary layer, used to validate the spanwise uniform version of the linking equation. Section III discusses a variety of techniques used to reduce data, focused on removing various contamination present in the aerooptical data and extracting correct convective velocity profiles. Section IV will present results derived from canonical turbulent boundary-layer experiments and compare them with the direct measurements using a hot wire. Finally, conclusions to this work will be given in Sec. V.

II. Experimental Setup

A. Facility

Detailed description of the experimental setup and procedure is provided in [19], so only essential information is presented here. Experimental measurements were conducted at the White Field facility at the University of Notre Dame. The facility is a Mach 0.6 closed-circuit wind tunnel powered by a 1750 hp variable rpm ac motor. The tunnel test section is 2.74 m in length with a 0.91×0.91 m square cross-section. Each of the four sides has three windows that are 0.6×0.6 m and are designed to give flexible optical access to the tunnel.

To create a canonical turbulent boundary layer, a boundary-layer development plate was designed to fit the facility. To avoid flow distortions in the inlet and exit regions, the plate was specified to be 2.13 m in length with 0.3 m of separation up- and downstream from the edge of the testing region. The plate itself is 2.54 cm thick, 0.89 m in width, and made entirely of aluminum. Figure 1a shows a CAD model of the plate and the supports. The plate is sectional and consists of an elliptical leading edge with a 152 mm major axis and a 25 mm minor axis and eight hollowed-out sections that together form the 1.8×0.89 m main body. The main body is covered with four aluminum plates, 6 mm thick, that form the smooth surface for developing the boundary layer and hide the internal cavity which houses instrumentation. Small gaps 10 mm wide between the plate and the test section help mitigate the formation of corner vortices at the junction of the plate and the test section. To secure the main plate to the tunnel, a series of support legs is attached to the underside and elevates the plate into the freestream. The support legs have a NACA 0012 airfoil cross-section and are 0.3 m tall. Figure 1b shows the fully assembled plate mounted on its support legs.

Boundary layers, present on the side walls, also contribute to the overall aerooptical distortions in the spanwise direction. It follows from Eq. (3) that, because the spanwise correlation length is proportional to the boundary-layer thickness, $\Lambda_{\rho,z} \sim \delta$, the aerooptical signal in the spanwise direction is proportional to the square root of the propagation length in the spanwise direction, $\mathrm{OPD}_{\mathrm{rms}} \sim \sqrt{\delta L}$. At the same time, the aerooptical effects from the side-wall boundary layers depend only on the boundary-layer thickness, $\mathrm{OPD}_{\mathrm{rms,side}} \sim \delta$ [3]. The ratio between them becomes $\mathrm{OPD}_{\mathrm{rms,side}}/\mathrm{OPD}_{\mathrm{rms}} \sim \sqrt{\delta/L}$. If the boundary-layer development plate is much wider than the boundary-layer thickness, the aerooptical contribution from the side-wall boundary layers to the overall signal can be neglected. In this experiment, $\sqrt{\delta/L} \approx 0.15$, so the contaminating effects should be small. More discussion of the effects of the side-wall boundary layers on the presented results will be given later in this paper.

To compensate for the imbalance of blockage above and below the plate and achieve a zero streamwise pressure gradient on top of the plate, a pivoting trailing edge flap a 25 mm thick and 150 mm long was installed at the end of the plate. The flap hangs loosely on the back of the main plate and is connected to a hinged push rod that extends down through the bottom of the test section. The flap has a range of motion of ± 25 deg. A number of pressure taps were placed in the first and fourth plate covers to monitor the pressure gradient over the plate. At the beginning of each test, the flap was calibrated using these pressure ports to ensure that there was in fact a zero pressure gradient. With the tunnel running, an absolute pressure transducer (Omega, DPG1000AD-15A) was sequentially attached to the Tygon tubing running from each pressure tap and its pressure recorded. The pressure differential between the most upstream and the most downstream pressure location was found to be less than 350 Pa at the highest run Mach number of 0.35. Two nondimensional pressure gradient factors that are commonly used [20] are the Clauser pressure gradient, $\beta = (\delta^*/\tau_w)(dP/dx)$, and the viscous scaled pressure gradient, $p_x^+ = (\nu/\rho U_\tau^3)(dP/dx)$. Using a maximum

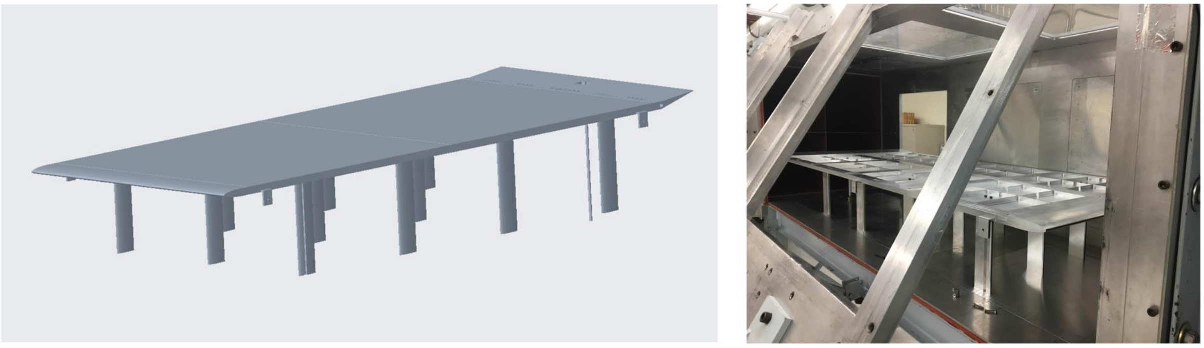

a) b)

Fig. 1 a) CAD model of the Whitefield Mach 0.6 wind-tunnel boundary development plate and b) assembled boundary-layer plate showing open cavities.

differential of 350 Pa across 1.5 m streamwise spacing between the pressure sensors yields $\beta = 0.037$ and $p_x^+ = 3.09 \cdot 10^{-5}$, indicating a negligible pressure gradient on top of the boundary-layer plate.

B. Optical Setup

The schematic of the optical measurements in the spanwise direction is shown in Fig. 2. A monochromatic light from a continuous a Neodymium-doped Yttrium aluminium Garnet (Nd:YaG) laser beam with wavelength of 532 nm was expanded to a collimated beam 25 mm in diameter. The collimated beam then passed through a pair of lenses that expanded or contracted the beam to the desired diameter, as will be discussed later. The expanded collimated beam was forwarded through the test section in the spanwise direction. Careful alignment was performed to ensure that the beam was parallel to the boundary-layer plate; see [19] for details. After passing through the flow of interest, the beam is reflected back along the same path it came from, using a return mirror on the opposite side of the test section. This so-called double-pass setup doubles the signal amplitude. The returning beam is split aside using a cube 50/50 beam splitter and, after proper reimaging, using a pair of reimaging lenses, is forwarded to a Shack–Hartmann wave front sensor. It consists of a Phantom v1610 high-speed camera with a lenslet array, attached in front of the imaging sensor. The lenslet array used in this study is a rectangular grid (70×60) of square lenses 0.3×0.3 mm, each with a focal length of 38.2 mm. All these components were assembled on an optical bench that sits on a series of slightly underinflated rubber bicycle tires to dampen most mechanical vibrations from the tunnel.

To investigate various spatial regions of the boundary layer, different lenses are used to change the ratio between the beam size traversing through the boundary layer and the beam size on the wave front sensor. This ratio is called magnification ratio Mag. The magnification ratios for a series of lens pairs can be computed as $\mathrm{Mag} = (F_1/F_2) \cdot (F_3/F_4)$. The various magnification ratios used in the boundary-layer experiments and their corresponding lens configurations are given in Table 1. Figure 3 illustrates how adjusting this magnification ratio maps the same spatial region seen by the camera to different parts of the boundary layer. The distance between the adjacent lenslet dots, when reimaged to the test section, represent the spatial resolution of the optical measurements. This spatial resolution is proportional to the magnification. For instance, with a magnification of 1, this distance is the same as the lenslet size, 0.3 mm, but with a magnification of 4, it becomes 1.2 mm. The summary of all test cases, including the run Mach number, sampling frequencies, and the spatial resolutions in the outer and inner units, are provided in Table 2.

C. Hot-Wire Anemometry

A Constant-Temperature Anemometry (CTA) hot wire was used to measure velocity statistics of the boundary layer created by the boundary-layer development plate at the location of the beam. The overheat ratio used was 1.8 with a sampling frequency of 30 kHz and a low-pass filter at 14 kHz. The wire length was 1.25 mm. The hot wire was calibrated in the range of Mach numbers 0.1–0.4, and the fourth-order polynomial fit was used for calibration. To calibrate the hot wire, the tunnel was run at known speeds, measured by a pitot probe placed in the freestream close to the hot wire, and voltage data from the anemometer were collected. A best fit of the data when plotting voltage versus the known velocity yields the calibration constants. Both pre- and postcalibrations were used to account for temperature drift in the tunnel, and a linear interpolation between the calibrations was used to compensate for the drift. To collect the velocity statistics inside the boundary layer, the hot wire was placed on a computer-controlled traverse system, capable of moving a hot wire in the wall-normal direction. Time series of the streamwise velocity were measured at 51 wall-normal locations with the sampling frequency of 30 kHz for 30 s. The first 11 wall-normal locations had an evenly spaced step size of 0.25 mm, the next 15 had a step size of 0.5 mm, and the last 25 had a step size of 1 mm. From the velocity data, both mean and fluctuating velocity profiles were extracted.

Table 1 Reimaging lenses used in boundary-layer studies

Magnification ratio, *Mag*	F_1/F_2, mm	F_3/F_4, mm	Test section beam size, mm	Camera beam size, mm
Mag = 1	$500/-250$	$400/800$	50	50
Mag = 1.6	$500/-250$	$400/300$	50	31.3
Mag = 4	$500/-250$	$800/400$	50	12.5

III. Data Reduction

A. Calculation of $\mathrm{OPD}_{\mathrm{rms}}$

Before we begin, let us recall that for collimated beams OPD can be approximated as a conjugate of the wave front, $\mathrm{OPD} = -W$ [1], so the statistics of the wave fronts and OPDs, such as the spectra and root-mean values, are identical. For this reason, the wave fronts and OPD will be used as synonyms in this paper.

For each test case, time series of the dot pattern were recorded using the high-speed camera, and the instantaneous dot positions were extracted in postprocessing using the centroiding algorithm [21]. Knowing the lenslet focal length and the magnification rate, the instantaneous dot positions were converted into the time series of deflection angles in the streamwise and the spanwise directions at various spatial points. Only the streamwise deflections angles, denoted $\theta(x, y, t)$, were used to analyze the aerooptical distortions.

The spanwise-uniform form of the linking equation, Eq. (5), relates $\mathrm{OPD}_{\mathrm{rms}}(y)$ to the spatial statistics of the density field at a given wall-normal location. Thus, we need to correctly compute the time average of spatial root mean square of the wave fronts, $\mathrm{OPD}_{\mathrm{rms}}(y) = \sqrt{\overline{\langle \mathrm{OPD}^2(x, y, t)\rangle_x}}$, where the overbar denotes the time averaging and angular brackets indicate the spatial averaging along the streamwise direction. Keep in mind that Eq. (5) is only valid for very large apertures, while the collected wave fronts were measured over a finite aperture of approximately one boundary-layer thickness. Finite aperture effects have been extensively studied by other researchers [3,22,23], and it was demonstrated that a finite

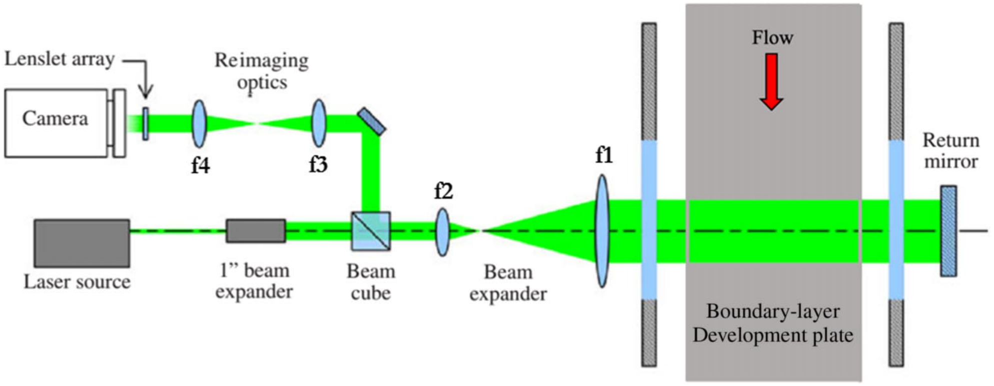

Fig. 2 Schematic of the optical setup using Shack–Hartmann wave front sensor.

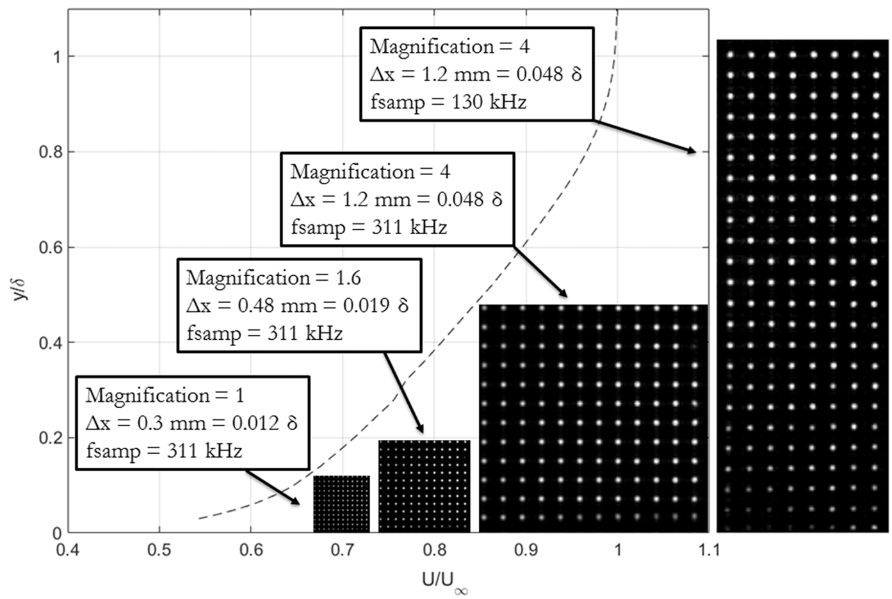

Fig. 3 Adjusting optical magnification to focus on different parts of the boundary layer.

Table 2 Test cases and corresponding optical resolution parameters

Test case	Mach number	Wall-normal extent and spatial resolution in outer units δ	Wall-normal extent and spatial resolution in inner units +	Sampling frequency, kHz
Mag = 1.0	0.35	0.12δ ($\Delta = 0.012\delta$)	680+ ($\Delta^+ = 68$)	311
Mag = 1.6	0.3	0.19δ ($\Delta = 0.019\delta$)	1090+ ($\Delta^+ = 109$)	311
Mag = 4.0	0.3	0.48δ ($\Delta = 0.048\delta$)	2740+ ($\Delta^+ = 274$)	311
Mag = 4.0	0.3	1.06δ ($\Delta = 0.048\delta$)	6042+ ($\Delta^+ = 274$)	130
Hot wire	0.3	1.2δ ($\Delta = 0.01\delta$)	6840+ ($\Delta^+ = 57$)	30

aperture acts as a high-pass filter and results in underpredicting the true large-aperture $\mathrm{OPD}_{\mathrm{rms}}$. This is a consequence of removing the instantaneous piston and tip/tilt components from the wave front. The tip/tilt components are typically corrupted by mechanical vibration and other experimental noise sources and often removed from the measured wave fronts.

An alternative approach to compute $\mathrm{OPD}_{\mathrm{rms}}$ is to recognize that the aerooptical distortions convect in the streamwise direction. Let us recall that the streamwise deflection angle is the derivative of the wave front, $\theta = \partial\mathrm{OPD}/\partial x$. In the convective case, the spatial derivative can be replaced with the temporal derivative, becoming related to the wave front as [24]

$$\mathrm{OPD}(x = U_c t) = -U_C \int_0^t \theta(\tau)\,\mathrm{d}\tau \tag{7}$$

Equation (7) means that a time series of deflection angles can be integrated in time to reconstruct OPD at that point in space, if the convective velocity U_C is known. It is more convenient to rewrite Eq. (7) in the spectral form, resulting in a relation between the wave front and the deflection angle autospectral densities,

$$S_W(f) = U_C^2 \frac{S_\theta(f)}{(2\pi f)^2} \tag{8}$$

Finally, $\mathrm{OPD}_{\mathrm{rms}}$ can be computed from the deflection angle autospectral density as

$$\begin{aligned}\mathrm{OPD}_{\mathrm{rms}}^2 &= \int_{-\infty}^{\infty} S_W(f)\,\mathrm{d}f = U_C^2 \int_{-\infty}^{\infty} \frac{S_\theta(f)}{(2\pi f)^2}\,\mathrm{d}f \\ &= 2U_C^2 \int_0^{\infty} \frac{S_\theta(f)}{(2\pi f)^2}\,\mathrm{d}f\end{aligned} \tag{9}$$

The immediate item of note in this equation is the factor of f^2 in the denominator. It means that any contamination of the deflection angle spectrum at low frequencies will be divided by the small $(2\pi f)^2$-factor and, as a consequence, will be greatly amplified, resulting in inaccurate estimates of both the wave front spectra S_W and the corresponding $\mathrm{OPD}_{\mathrm{rms}}$ values. If we make a physically reasonable assumption that in the limit as frequency approaches zero S_W approaches some finite constant (which was verified in numerical simulations of optical distortions in turbulent boundary layers [17]), then the deflection angle spectrum at low frequencies should behave as $S_\theta \sim f^2$. This requirement can be used to estimate the spectrum behavior of low frequencies. On the other hand, the wave front spectrum is much less affected by any potential contamination at high frequencies, as the corresponding portion of the S_θ spectrum, which is already small, is further divided by a large $(2\pi f)^2$ factor.

Thus, various sources of contamination, predominantly at the low frequencies, should be properly removed from the deflection angle spectra in order to correctly compute $\mathrm{OPD}_{\mathrm{rms}}$. A method developed in [25] was originally introduced to mitigate this corruption. The method uses several spatial correlations of deflection angles at varying separations to split the measured spectrum into a convective component and a stationary component. In other words, by having additional redundant data sets all collected at the same instant in time, it becomes possible to sort out components of the signal that only depend on space (stationary) from those that vary with space and time (convective). The only assumption involved in this method is that the spectrum has only two components, the stationary and the purely convective ones. Equations (10) and (11) show the decomposition of the Fourier transform of deflection angles $\hat{\theta}(x, f)$ and the resulting cross spectral correlation $S(\Delta x, f)$,

$$\hat{\theta}(x, f) = \hat{\theta}_S(f) + \hat{\theta}_C(f)\exp\left(2\pi \mathrm{i} f\left[t - \frac{x}{U_C}\right]\right) \tag{10}$$

$$S_\theta(\Delta x, f) = \frac{\langle \hat{\theta}(x,f)\hat{\theta}^*(x+\Delta x, f)\rangle}{T} = S_S(f) + S_C(f)\exp\left(\frac{2\pi \mathrm{i} f \Delta x}{U_C}\right) \tag{11}$$

where T is the Fourier transform block time, S_S is the stationary power spectrum, S_C is the convective power spectrum, and the asterisk denotes the complex conjugate. With multiple spatial separations, Eq. (11) is overdetermined, and a least-squares solution can be obtained at each frequency for S_S and S_C. A representative example of this decomposition is shown in Fig. 4. It can be seen that the low-end buildup due to mechanical vibration was significantly removed from the convecting portion of the spectrum and the theoretical slope of f^2 was recovered to some degree. In a few cases, the multipoint decomposition was not able to totally remove the low-end corruption, but in general, it worked effectively, and because of this, the convective portion will be used in instead of the original deflection angle spectrum for all further analysis.

Figure 4 also shows that there still remains a significant drop off in spectral content at the high end of the spectrum compared to the expected theoretical $f^{-4/3}$ slope [2,26]. The most likely cause of this high-frequency damping is signal attenuation due to a finite subaperture size. A theoretical estimation of how averaging over the span of a subaperture affects the deflection angle spectrum is given in [26]. It is important to note that the multipoint decomposition is unable to recover the high-end theoretical slope, but, as mentioned before, it should not significantly affect the extracted $\mathrm{OPD}_{\mathrm{rms}}$ values.

In an attempt to minimize the corrupting effects at both the low and the high frequencies in order to correctly estimate $\mathrm{OPD}_{\mathrm{rms}}$ values from the experimentally measured deflection angle spectra, a simple semi-empirical model was used in [27] to approximate the shape of S_θ using the theoretical considerations of the low- and high-frequency tails. The functional form of the model was adapted in the current work to further clean up the low-end corruption of the convective component of the deflection angle spectra. The model uses the peak amplitude $S_{\theta,\mathrm{peak}}$ and the peak frequency f_{peak}, both of which are generally isolated from areas of the spectrum that are corrupted. The model is as follows:

$$S_\theta(f,y) = S_{\theta,\mathrm{peak}}(y)\frac{6.00}{f^2_{\mathrm{peak}}(y)}\left[\frac{f}{1+[1.25f/f_{\mathrm{peak}}(y)]^{5/3}}\right]^2 \tag{12}$$

The model was used to clean up only the low-end of the spectrum by replacing the part of experimentally measured spectrum below the peak frequency with the model fit. The spectrum above the peak frequency was kept unchanged. The benefit of this approach is that it removes remaining corrupting influences at the low end of the spectrum, using peak quantities in the middle of the spectrum, where the corruptions are minimal. Figure 5 demonstrates the model fit of Eq. (12) for selected wall-normal locations using the peak values of the convective spectra from the multipoint decomposition. By design, the model removes any residual contaminations at the low frequencies, while remaining faithful to the central and high-end portions of the spectrum. This can be clearly seen in the spectrum at $y/\delta = 0.1$, where the convective component (a solid red line) still has significant buildup at the low frequencies, which would result in an unrealistically large value of $\mathrm{OPD}_{\mathrm{rms}}$. The model fit (a dashed red line) guarantees that the resulting wave front spectrum stays finite at low frequencies.

The presented model fit was implemented to all extracted convective components of the deflection angle spectra, and the corresponding $\mathrm{OPD}_{\mathrm{rms}}(y)$ profiles were computed using Eq. (9). These profiles were used to estimate the density correlation lengths $\Lambda_{\rho,z}(y)$ via Eq. (6). In addition, $\theta_{\mathrm{rms}}(y)$ profiles were calculated by integrating the modeled deflection angle spectra.

B. Convective Velocity

One of the major motivations behind this study is developing a technique that is capable of measuring convective velocity nonintrusively. Also, to correctly compute $\mathrm{OPD}_{\mathrm{rms}}(y)$ profiles, using Eq. (9), the values of the local convective speed are needed. Two methods of extracting the convective speeds will be presented in the following: the spectral cross-correlation method and the dispersion method.

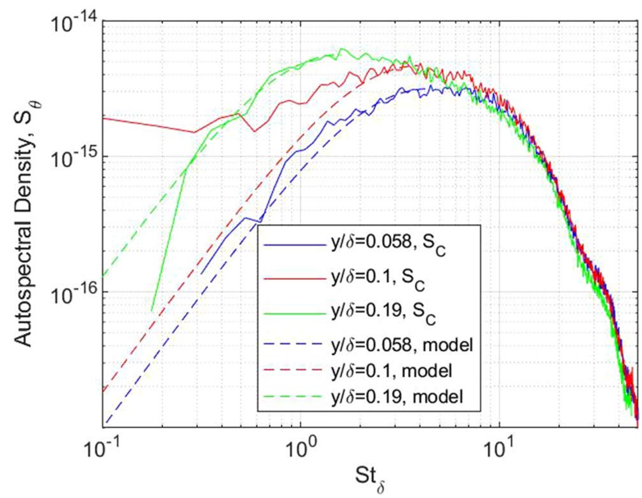

Fig. 5 The convective components and the low-end models of S_θ from Eq. (12) using the Mag 1.6 data set as an example.

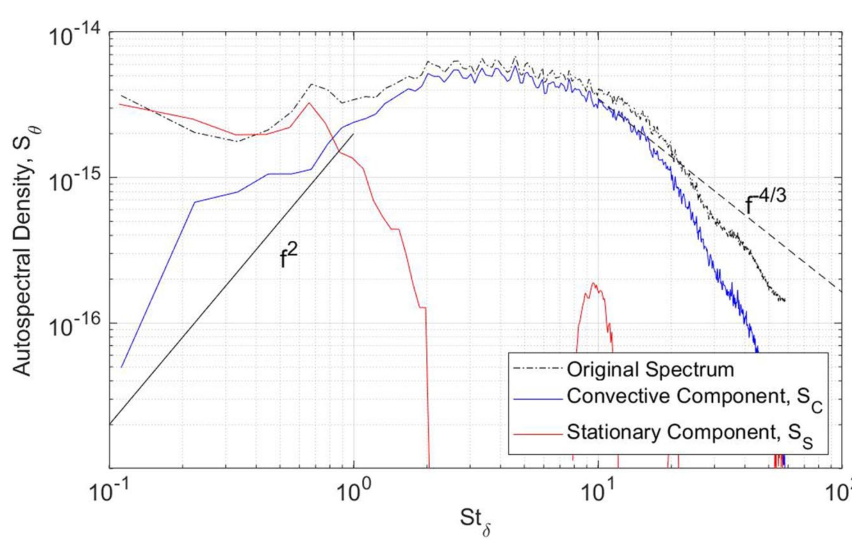

Fig. 4 Breakdown of the total deflection angle spectrum into convective S_C and stationary S_S components.

The spectral method was introduced in [28] and uses the deflection angles in two spatial points, separated by the distance Δx. From Eq. (11), it follows that the argument (phase) of the spectral cross-correlation spectrum is a linear function of the frequency, and the phase slope is related to the convective speed. The convective speed can be calculated from the phase slope because $dArg[S(f)]/df = 2\pi\Delta x/U_C$. This approach was demonstrated to provide good results if the deflection angles are sampled sufficiently fast and the separation between beam is small enough [28].

With the use of a Shack–Hartmann sensor, multiple streamwise correlations can be made at different Δx. Figure 6 shows the scaled phase $Arg[S(f)]/\Delta x$ for five different Δx values. Figure 6 shows collapse for all Δx up to almost 50 kHz. However, the phase slope does not agree with the expected slope, based on the direct measurements of the velocity using a hot wire, shown as a straight black line in Fig. 6. This discrepancy was traced to insufficient spatial resolution, which will be further clarified later in this paper. As a result, the spectral cross-correlation was corrupted by spatial aliasing effects and resulted in biased estimates of the phase slopes.

The spectral method uses frequency analysis and spatial averaging. In contrast, the dispersion method uses both frequency and spatial information in the form of a two-dimensional (2-D), frequency/wave number spectrum. Given a row of deflection angle data at constant height $\theta(x,t)$ a 2-D Fourier transform yields $S_\theta(k_x, f)$. In general, 2-D spectral analysis of a convecting quantity yields a spectrum with a linear ridge, the slope of that ridge corresponds to the convective velocity, $U_C = 2\pi f/k_x$. If other optical structures, moving at a different speed, are present along the beam, it will result in the appearance of another branch with a different slope. The ability of the dispersion method to identify different convective speeds can be used to isolate and study the corresponding optical structures. This approach was successfully implemented to isolate and study aeroacoustical contamination from jet engines present in the aerooptical data in flight [29].

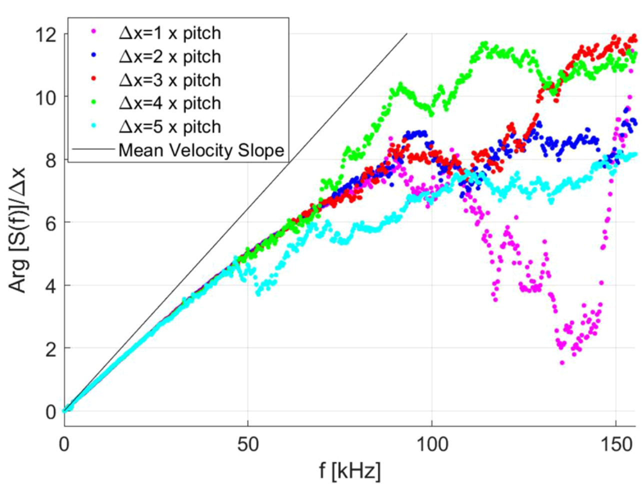

Fig. 6 Phases of the spectral cross-correlation functions for different Δx at $y/\delta = 0.1$. Expected phase slope based on the velocity measured using hot wire is also presented.

With proper sampling frequency and spatial resolution, this spectrum would be properly resolved and would look similar to Fig. 7a. A linear fit to the ridge of the 2-D spectrum is the most common method of computing convective velocity. Traditionally, the peak spectral value is used in determining the ridge; however, del Álamo and Jiménez [30] proposed using the spectrum's center of gravity to define the ridge to more accurately account for the contributions from all scales. This second approach was implemented in these studies.

An idealized spectrum for a continuous 2-D Fourier transform (an infinite sampling frequency and wave number) is shown schematically in Fig. 7a as a single branch with a constant slope, determined by the convective speed. For simplicity, consider aliasing in space only. If the signal is sampled at a finite wave number, $k_{\max} = 2\pi/\Delta x$, the Nyquist–Shannon sampling theorem states that the resulting discrete spectrum will be a superposition of infinite number of continuous spectra, periodically shifted by $n \cdot k_{\max}$, where n is an integer number, as illustrated in Fig. 7b. If the original spectrum has spatial content above the Nyquist wave number, $k_{\max}/2$, it will result in shifted branches entering the range of spatial wave numbers $[-k_{\max}/2, +k_{\max}/2]$, as shown inside the rectangular box in Fig. 7b. This is a classic example of aliasing in discrete 2-D Fourier transforms.

Understanding the origin of the aliasing provides a practical way to remove it. The algorithm is demonstrated in Fig. 8. Consider a discrete 2-D spectrum, aliased in space, as shown in Fig. 8a. This can be shifted by $\pm k_{\max}$, $\pm 2k_{\max}$, and so on, and stacked left and right of the discrete spectrum, as demonstrated in Fig. 8b. This leads to the main branch recovering its original shape, and the slope of the main branch can be studied. By applying a band filter, the main branch can be isolated and analyzed. This stacking approach, but performed in the frequency direction, was implemented to recover the spectra of the deflection angles of hypersonic boundary layers beyond the Nyquist frequency [31].

To illustrate this algorithm, a set of experimentally obtained data for Mag = 4 is used as an example. Using a streamwise row at $y/\delta = 0.1$, the 2-D spectrum S_θ was computed. The particular data set, shown in Fig. 9, has ten streamwise points and a sampling frequency of 311 kHz. The log of the computed dispersion plot is given in Fig. 9a. The main convective branch impacts the wave number limit at about 25 kHz and is aliased to the left edge of the plot. Figure 9b shows the same data reconstructed using the stacking method. The main convective branch is clearly resolved out to triple the spatial Nyquist limit. Independently measured mean velocity, using a hot wire, can be used to calculate an expected slope to compare to the ridge slope in this dispersion plot. This was demonstrated in Fig. 9b, in which the main convective branch remains linear and follows the mean velocity slope out to 75 kHz, which encompasses the entirety of the spectrum.

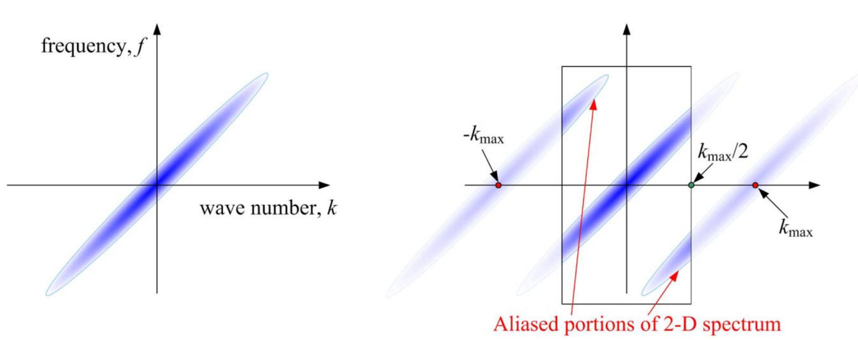

a) Continuous 2-D fourier transform **b) Discrete 2-D fourier transform**

Fig. 7 Schematic illustrating temporal aliasing of convective 2-D spectra with insufficient sampling wave number.

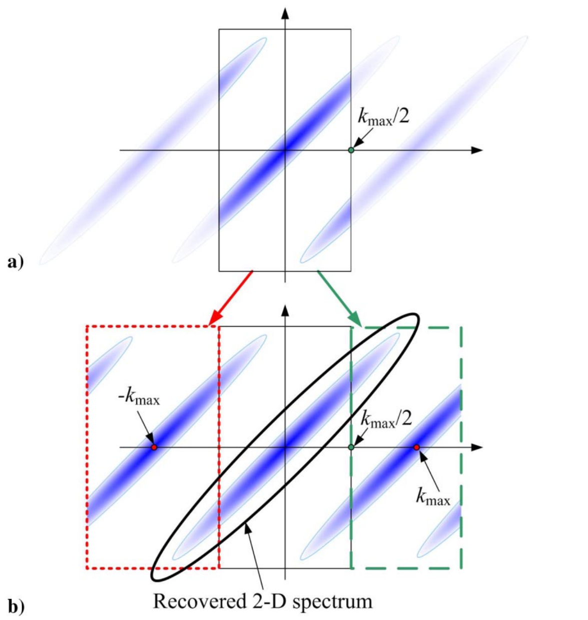

Fig. 8 Schematic illustrating a proposed dealiasing stacking algorithm to recover the 2-D spectrum.

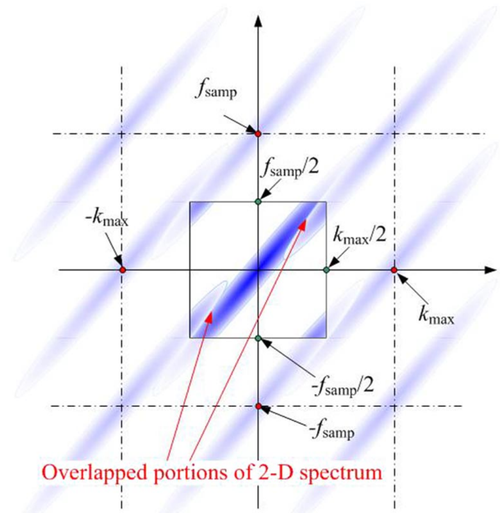

Fig. 10 Schematic illustrating the situation when $U_C \approx 2\pi f_{samp}/k_{max}$, corresponding to $\Gamma = f_{samp}\Delta x/U_C \approx 1$, which results in an inseparable overlap in the discrete 2-D spectrum.

It is straightforward to see that this method fails when the Nyquist angular frequency divided by the maximum resolved wave number is approximately equal to the local convective velocity, $U_C \approx 2\pi f_N/(k_{max}/2) = f_{samp}\Delta x$; in other words, when the main branch goes directly into the corner of the sampling window. If this is the case, the positive and negative branches might overlap at the tails and become inseparable, as illustrated in Fig. 10. In fact, this can limit the usable portion of the spectrum to even below the spatial and temporal Nyquist frequencies. To avoid this issue, a constant Γ is introduced, which relates the sampling frequency and the separation between points in space $\Gamma = f_{samp}\Delta x/U_C$. For the case when the ridge hits the corner of the dispersion plot, $\Gamma \approx 1$. To avoid this tail overlap, Γ should be larger than 2 or less than 0.5. This large margin helps to account for the fact that U_C is an unknown and often only a ballpark estimate can be made.

Recalling the nonlinearity observed in phase of the spectral method, Fig. 6, the aliasing in the k_x direction is expected as the root cause and ultimately the flaw of a simple spectral cross-correlation analysis. To examine this further, the two-point spectral cross-correlation phase, shown in Fig. 6, is shown again in Fig. 11a. Note that the axes in this plot have been flipped from the typical way in which phase is plotted so that the frequency axis is the same as in the dispersion plots. Examining Fig. 11a, we see that the slope of the phase data begins to deviate from that associated with the mean velocity, measured by a hot wire, around 20 kHz. The same data set was used to perform the dispersion analysis and presented in Fig. 11b. It is clear that no such deviation exists. Because of this, it is expected here that the spatial aliasing is directly responsible for the phase deviating from a linear slope in the spectral cross-correlation method.

C. Clauser Method to Compute Local Skin Friction

The Clauser method of computing the local skin friction from the mean velocity profile is based on the assumption that a similarity exists linking the inner near wall region with the outer velocity defect region [32]. Based on dimensional analysis, Clauser showed that the near-wall inner layer

$$U^+ = \frac{U}{u_\tau} = y^+ = \frac{y u_\tau}{\nu}$$

and the outer layer

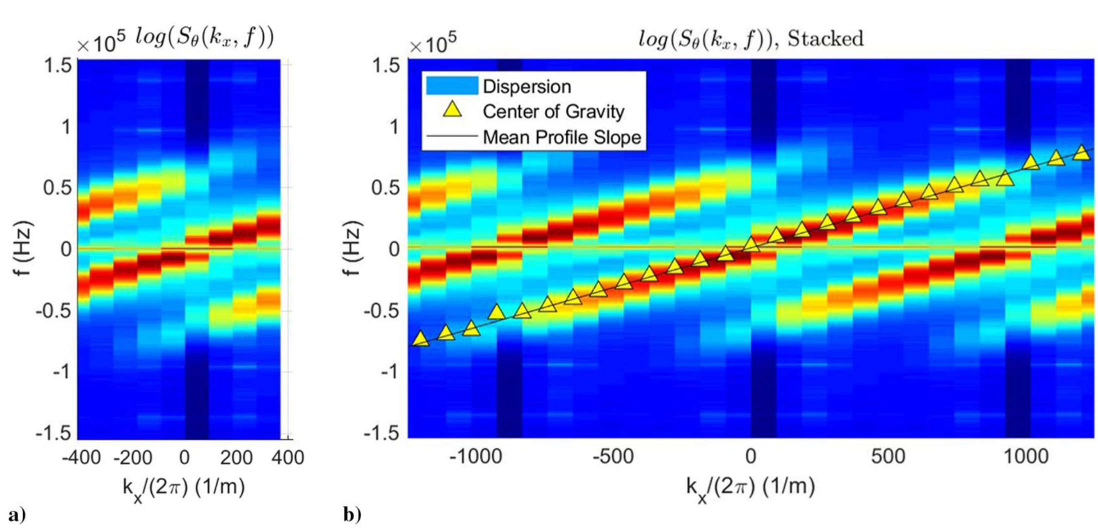

Fig. 9 a) unaltered 2-D dispersion plot of the Mag = 4, 311 kHz data set and b) reconstructed (stacked) 2-D spectrum. The center-of-gravity method is shown along with the corresponding slope of the hot-wire mean velocity. The wall-normal location is $y/\delta = 0.1$.

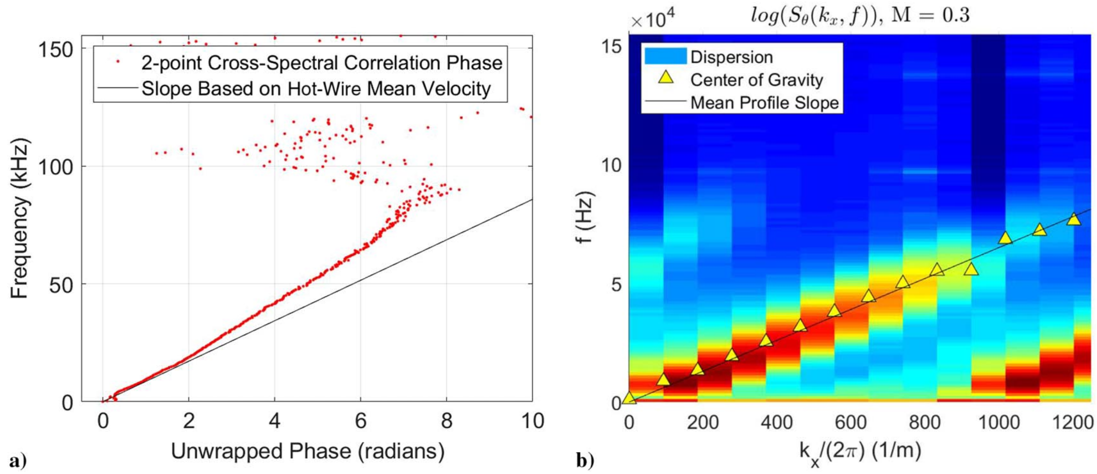

Fig. 11 a) phase of the spectral cross-correlation from Fig. 6 with switched axes for better comparison to dispersion plots and b) a first quadrant of the reconstructed 2-D dispersion plot of the same data set. The wall-normal location is $y/\delta = 0.1$.

$$\frac{U - U_\infty}{u_\tau} = f(y/\delta)$$

must have a region of overlap between them that is a function of the freestream velocity, boundary-layer thickness, and viscosity, the three variables that are in only one of those two equations. Townsend [33] built upon Clauser's observation and proposed a similarity hypothesis that states that surface conditions set the wall shear stress and boundary-layer thickness and then the outer layer turbulence simply adjusts accordingly. This adjustment behaves in a universal and self-similar manner. This resulted in the form of the so-called log/law as it is commonly reported,

$$U^+ = \frac{U}{u_\tau} = \frac{1}{\kappa}\ell n(y^+) + B = \frac{1}{\kappa}\ell n\left(\frac{yu_\tau}{\nu}\right) + B \tag{13}$$

where κ and B are experimentally determined constants. Nagib and Chauhan [34] provide an excellent overview of the reported values in the literature. In this study, values of $\kappa = 0.385$ and $B = 4.1$ were chosen, consistent with the zero pressure gradient turbulent boundary-layer studies [35,36].

To compute u_τ and C_f from Eq. (13), it must first be rearranged. Multiplying both sides of the equation by u_τ/U_∞ yields

$$\frac{U(y)}{U_\infty} = \left[\frac{1}{\kappa}\frac{u_\tau}{U_\infty}\right]\ell n\left(\frac{yU_\infty}{\nu}\right) + \left[\frac{1}{\kappa}\frac{u_\tau}{U_\infty}\ell n\left(\frac{u_\tau}{U_\infty}\right) + B\frac{u_\tau}{U_\infty}\right] \tag{14}$$

Equation (14) is now in a form where measured $U(y)$ can be plotted versus y with known U_∞ and ν. The slope of the linear portion of this plot uniquely defines u_τ. Knowing the skin friction velocity, the local skin friction C_f can be computed by recalling that for incompressible flows $C_f = 2(u_\tau/U_\infty)^2$.

The assumptions embedded in this analysis are that the flow is in equilibrium, meaning a constant stress profile; κ and B are in fact accurate to the particular Reynold's number and flow geometry; and the Reynold's number is large enough that a linear log region exists over a range of y^+ values so that a slope can be defined. As Reynold's number increases, scale separation between the near-wall dissipative eddies and the outer region turbulence generation eddies grows. Wei et al. [37] examined a number of low Reynold's number experiments and concluded that an error in u_τ of up to 5% was possible for $Re_\theta = 500$ but that this error diminished beyond $Re_\theta = 1340$.

IV. Results

A. Deflection Angle Spectra

The convective deflection angle spectra were extracted from all test cases at different wall-normal coordinates. Figure 12 plots the convective portion of the spectrum from Eq. (11) along with the peak value at each wall-normal location for all three magnifications. When combining the cases, preference was given to the lowest magnification at each height in the boundary layer. In general, the peak values for all magnification rates agree with each other within the scatter of the data. Using the spectra, we can associate a length scale to the frequencies containing the most energy. For example, above $y/\delta = 0.3$, the peak value of S_θ remains relatively constant at a Strouhal number of 1. This indicates that the length scale that is most strongly energetic toward S_θ at those wall-normal locations is roughly the boundary-layer thickness. However, very close to the wall, the peak is at a higher Strouhal number, about 10, indicating smaller structures.

Besides the peak Strouhal number being a function of the wall-normal location, Fig. 12 provides additional insight by looking at the amplitude of the main peak of S_θ. Very near the wall, the peak amplitude is rather low, which means that while the smaller structures are contributing most to the energy in the spectrum each individual scale is contributing less relative to the larger outer structures. Moving away from the wall, the amplitude of the mean peak increases, and the mean peak location shifts to lower frequencies, indicating larger and more energetic optical structures. At a point near the edge of the boundary layer, roughly $y/\delta = 0.7$, the magnitude of the mean peak begins to decline, while the peak location remains constant. This decline in the mean peak amplitude also leads to the reduction of the overall total energy $\theta_{\mathrm{rms}}(y)$ presented in Fig. 13. The overall decline is most likely due to intermittency effects, which will be discussed later in this paper.

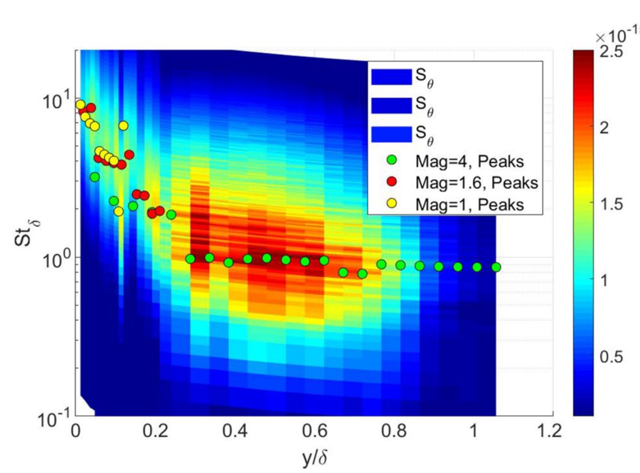

Fig. 12 Evolution of deflection angle autospectral density combined for all magnification cases. The spectral peak values at each wall-normal location for all three magnifications are also indicated by symbols.

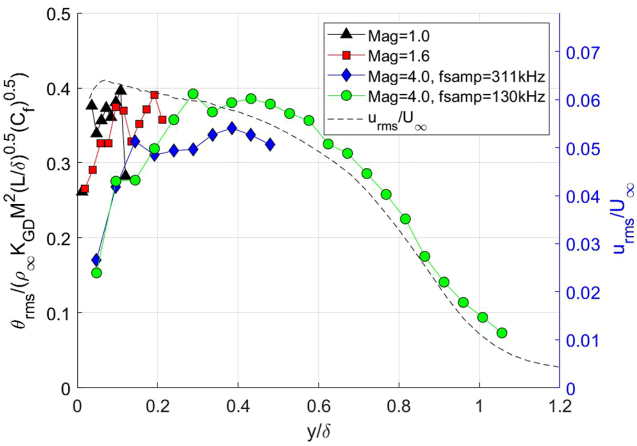

Fig. 13 Normalized $\theta_{\mathrm{rms}}(y)$ profiles for all test cases. The fluctuating velocity profile u_{rms} is also plotted for comparison.

B. Convective Velocity

1. Hot-Wire Measurements

The wall-normal profiles of the mean and the fluctuating component of the streamwise velocity, measured using a hot wire, are presented in Fig. 14. The mean velocity profile shows a presence of a canonical boundary layer with a log-linear region with constants $C = 3.1$ and $\kappa = 0.385$. Note that the viscous subregion and a portion of the buffer region of the boundary layer are not resolved due physical constrains to place the hot wire very close to the wall. Using the mean velocity profile, several parameters for the boundary layer were calculated and are given in Table 3. The hot-wire length used in the experiments was 1.25 mm. This length, expressed in inner units, results in a hot wire l^+ for this experiment of nearly 300, far higher than the recommended value of $l^+ < 20$ [38]. The result of the large hot-wire length is a dampening in the perceived turbulent fluctuations due to spatial averaging along the wire. In addition to spatial averaging, the relatively low low-pass filtering at $f_{\mathrm{cut}} = 14$ kHz corresponds to the normalized sampling time of $\Delta t^+ = u_\tau^2/(f_{\mathrm{cut}}\nu) \sim 50$, which is not sufficiently small to temporally resolve all turbulent structures [38], further reducing the measured turbulent fluctuations. To illustrate the impact, properly spatially and temporally resolved ($l^+ < 20$, $\Delta t^+ < 1$) turbulence intensity profiles presented in [38] were interpolated for the current Re_τ and plotted in Fig. 14. The severity of the spatial attenuation is clear, considering that deviation from the fully resolved curve extends all the way to $y^+ = 3000$, well beyond the log region. At $y^+ = 1000$, the attenuated turbulence intensity is 75% of the resolved data. The strong Reynold's analogy, which will be used to relate density and the velocity statistics later in this paper, relies on the correct fluctuating and mean velocity profiles to predict the fluctuating density profiles. Using the present attenuated fluctuating velocity profile would result in significant errors, and therefore it was decided that all calculations involving the fluctuating velocity will use the fully resolved data presented in [38]. Note that the spatial averaging affects only the fluctuating velocity profile, as the mean profile agrees with each of the ones available in the open literature.

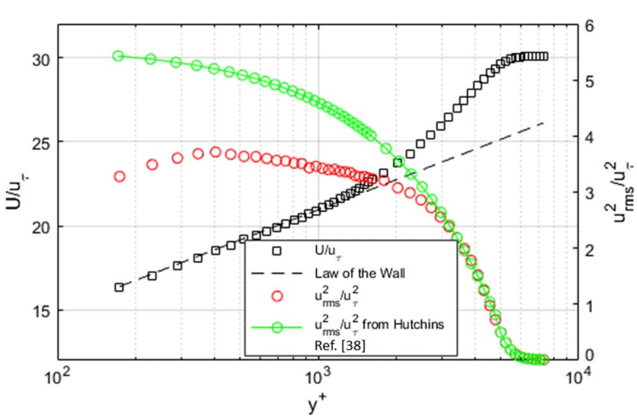

Fig. 14 Hot-wire mean and rms profiles plotted in inner units. RMS profile taken from Hutchins et al. [38] shows the near-wall attenuation.

2. Convective Velocities Using Spectral Cross-Correlation and Dispersion Methods

Strictly speaking, the convective velocity is not equal to the local mean velocity [30,39,40]. Del Álamo and Jiménez [30,41], in their computational work on channel flows, found that the convective velocity near the wall appears to asymptote to a nonzero constant. In addition, decomposing the convective velocity into large and small wavelengths revealed that the largest wavelengths convect at a nearly constant velocity independent of wall-normal location and the small wavelengths generally follow the mean velocity everywhere except near the wall. In a similar study using PIV, LeHew et al. [42] found agreement with the results of del Álamo and Jiménez. Geng et al. [39] and Liu and Gayme [40] built upon this work and have shown that the average convective velocity asymptotes to approximately $10u_\tau$ at the wall beginning at $y^+ < 20$. Liu and Gayme particularly looked at the influence of streamwise and spanwise wave number and found evidence of large-scale interactions with the small scales in the viscous sublayer consistent with Hutchins and Marusic [43]. The largest contributors to convective velocity in the viscous sublayer were structures on the order of the buffer layer height, yet even larger structures had nonnegligible contributions.

All the aforementioned studies point out that the deviation of the convective speed from the mean velocity and its dependence of the spatial wave number was observed only near the wall, $y^+ < 20$–30. In the present studies, however, the nearest resolved point in the wall-normal direction was $y + \sim 60$; see Table 2. Based on the discussion in the previous paragraph, away from the wall, the convective velocity should be equal to the mean velocity. Therefore, the convective velocity, obtained via optical methods, should agree with the mean velocity, measured by the hot wire. The results from multiple optical data sets were analyzed using both the spectral cross-correlation method and the dispersion method to extract the local convective speeds, and the results are presented in Fig. 15. The spectral cross-correlation method in Fig. 15 uses frequency limits of 10–25 kHz to define the slope fitting region. The convective velocities are scaled using u_τ computed from the hot-wire mean velocity profile and Clauser method. It is immediately clear that the spectral cross-correlation method overpredicts the mean velocity profile throughout the entire boundary-layer region for all cases. The dispersion analysis, presented in the previous chapter, revealed that spatial aliasing led to the nonlinearity in the observed phase plots. The overshoot of the spectral cross-correlation method in Fig. 15 suggests that this spatial aliasing biases the profiles toward the larger, faster-moving structures. On the other hand, the dispersion method does a good job of following the mean profile over a wide range of y^+ between 200 and 3000. The discrepancy above $y^+ = 3000$ is most likely due to intermittency effects, which will be addressed in the next paragraph. Very near the wall, $y^+ < 200$, the dispersion-based convective velocities approach a constant. This is most likely due to spatial averaging

Table 3 Turbulent boundary-layer parameters

Mach number	Boundary-layer thickness δ	Freestream velocity U_∞	Friction velocity u_τ
0.3	25 mm	100.8 m/s	3.35 m/s
Re_δ	Re_θ	Re_τ	H-factor
$1.71 \cdot 10^5$	19,975	5,775	1.33

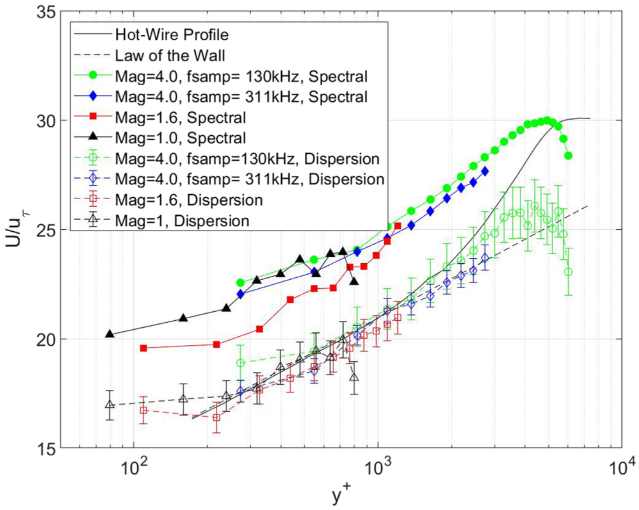

Fig. 15 Comparison of spectral and dispersion methods computation of convective velocity in inner units. Closed symbols are the spectral method, and open symbols are the dispersion method. The mean velocity profile from hot wire is also presented for comparison.

over subapertures. The small scales in the boundary layer are smaller than the subaperture size at this location, and as such, the apparent convective velocity is biased toward the larger, faster-moving structures. Based on the suggestions in [25], the subaperture size Δx should be less than $(\delta/St_{\delta,\mathrm{peak}})(U_c/U_\infty)$, to accurately resolve the convective velocity of the scales of interest. For the current data near the wall, the peak Strouhal number is approximately 4, and the expected convective velocity is roughly 0.5 of the freestream velocity based on the hot-wire velocity profile at the nearest wall-normal location measured. This gives a maximum subaperture size of $\Delta x = 0.15$ mm, which is half the size of the smallest subaperture used in this work. As the main portion of interest at the outset of this work was the log region of the boundary layer, these larger subapertures were acceptable; however, for anyone who is interested in regions of the boundary layer closer to the wall, the subaperture size must be chosen small enough for accurate measurement of convective velocity in this region.

From Fig. 15, it is clear the dispersion analysis consistently underestimates the convective velocity in the wake region of the boundary layer above $y^+ > 2000$. To understand it, let us recall that from an optical point of view the only parts of the flow contributing to the optical signal are those which contain density fluctuations. Intermittency in a boundary layer helps to describe the interface between the turbulent flow and the laminar freestream. This interface fluctuates as turbulent bursts reach out into the freestream. The intermittency function describes the fractional percentage of time that a particular wall-normal location is turbulent. Because the laminar freestream has no density fluctuations, only those portions of time that are turbulent contain density fluctuations. As intermittency begins to set in at roughly $y/\delta = 0.5$, turbulent bursts into the freestream become more and more infrequent. To illustrate this, Fig. 16 replots the velocity profiles extracted using the dispersion method in Fig. 15 in outer units. The intermittency function computed from the corresponding hot-wire data is overlaid on the same plot. The point at which the convective velocity profiles begin to diverge from the hot-wire mean profile coincides with the onset of intermittency. Thus, the deviation of the optically extracted convective velocities from the true velocities can be attributed to intermittency effects, where the optical sensor does not *see* the laminar parts of the boundary layer. Because these laminar regions move faster than the turbulent regions, it results in underpredicting the values of the convective velocity. This result also suggests that the turbulent regions appear to move at a relatively constant convective velocity beyond $y/\delta = 0.6$. Also, it should be pointed out that outside the boundary layer the density fluctuations in the freestream are negligible, and the dominant optical source becomes the side-wall boundary layers. As a consequence, the convective speed outside the boundary layer decreases to approximately $0.8U_\infty$, which corresponds to the convective speed of the aerooptical

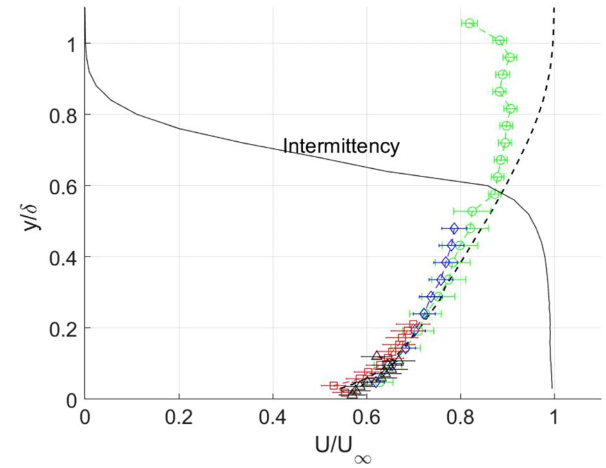

Fig. 16 Dispersion method convective velocity profiles from Fig. 15 in outer units. Intermittency function computed from hot-wire data overlaid to correlate with divergence from mean hot-wire profile.

distortions in the subsonic boundary layers, collected in the wall-normal direction [3]. With this in mind, care should be taken in equating optical convective velocity with the mean velocity in this region, dominated by intermittency effects. This a clear limitation of the presented optical technique to extract the convective speed in regions where intermittency (a mixture of laminar and turbulent flows) is dominant. The capability of nonintrusively measuring the mean velocity is a powerful tool, but it is limited to the flow regions with sufficient and predominantly turbulent fluctuations. Having said that, numerous applications are still unaffected by this constraint, and potentially the most powerful is the use of Clauser method.

3. *Optical Measurements of Local Skin Friction Coefficient*

After obtaining convective velocity profiles for all test cases, the Clauser method can be used to calculate the friction velocity u_τ using Eq. (14). By plotting $\ln(yU_\infty/\nu)$ versus U/U_∞, a linear regression analysis was used on the linear portion of the profile in a least-squares sense to obtain the slope and the related uncertainty. The slope is only a function of κ, u_τ, and U_∞, where the only unknown is u_τ. Table 4 shows the results of using Clauser's method as well as a 90% confidence interval for u_τ and C_f. Overall, most of the test cases give good estimates of u_τ and C_f, though test case Mag $= 4$ slightly underpredicts both. As can be seen from the percent errors, test case Mag $= 1$ and Mag $= 4$, $f_{\mathrm{samp}} = 130$ kHz have relatively high error bars. In test case Mag $= 1$, the large error was due to the dispersion ridge tails interacting with each other, with Γ constant being approximately 1, in which the dispersion method is less effective.

This presented optical approach demonstrates an opportunity to perform nonintrusive measurements of the velocity profiles in situations, where direct velocity measurements might be difficult or intrusive, for instance, at supersonic or hypersonic speeds. Also, it is straightforward to extend this technique to estimate the skin friction for rough-wall boundary layers.

C. Wall-Normal Distributions θ_{rms} and $\mathrm{OPD}_{\mathrm{rms}}$

Before presenting results for θ_{rms} and $\mathrm{OPD}_{\mathrm{rms}}$, the corresponding scaling laws are required. For the levels of aerooptical distortions in subsonic turbulent boundary layers in the wall-normal direction, a scaling law was introduced in [24], $\mathrm{OPD}_{\mathrm{rms}} = \beta\rho_\infty K_{\mathrm{GD}} M^2 \delta\sqrt{C_f}$, where β is an experimental constant. In the case of spanwise projection, the same scaling may not be appropriate, as $\mathrm{OPD}_{\mathrm{rms}}$ also depends on the spanwise length of the boundary layer, as shown in Eq. (6). Looking at this equation, it is reasonable to assume that the spanwise correlation length $\Lambda_{\rho,z}$ is proportional to the boundary-layer thickness δ. From here, it follows that $\mathrm{OPD}_{\mathrm{rms}} \sim \sqrt{\delta L}$. By comparing this scaling with the wall-normal scaling [24], it results in the following proposed scaling law for the $\mathrm{OPD}_{\mathrm{rms}}$ in the spanwise direction:

Table 4 Estimates of the skin friction coefficients from optical data using Clauser's method

Test case	Mach number	u_τ, m/s	Error in u_τ, %	$C_f x10^3$	Error in $C_f x10^3$, %
Mag = 1.0	0.35	3.72	1.12 (30)	2.00	1.20 (60)
Mag = 1.6	0.3	3.35	0.30 (9.0)	2.21	0.39 (18)
Mag = 4.0	0.3	3.00	0.19 (6.3)	1.77	0.22 (13)
Mag = 4.0 f_{samp} = 130 kHz	0.3	3.43	0.52 (15)	2.32	0.70 (30)
Hot wire	0.3	3.36	(7.9)	2.20	(15.8)

$$\mathrm{OPD_{rms}} \sim \rho_\infty K_{\mathrm{GD}} M^2 \sqrt{\delta L}\sqrt{C_f} \tag{15}$$

It should be understood that care needs to be taken comparing spanwise and wall-normal values of normalized $\mathrm{OPD_{rms}}$. If this general scaling is used in the wall-normal direction, $L = \delta$, and the scaling of δ used in [24] is recovered.

Recall that the deflection angle is a gradient of the wave front. If the wave front has a characteristic streamwise length scale Λ, then the level of streamwise deflection angle, characterized by temporal root-mean-square value θ_{rms}, is related to the amplitude of the wave front, characterized by $\mathrm{OPD_{rms}}$, as $\theta_{\mathrm{rms}} \sim \mathrm{OPD_{rms}}/\Lambda$. Because we can also assume that $\Lambda \sim \delta$, the resulting scaling law for the deflection angle becomes

$$\theta_{\mathrm{rms}} \sim \rho_\infty K_{\mathrm{GD}} M^2 \sqrt{L/\delta}\sqrt{C_f} \tag{16}$$

Using experimental data for different spatial resolution cases, wall-normal profiles for the normalized θ_{rms} were computed and are plotted in Fig. 13. At a glance, the profile looks qualitatively similar to a profile of turbulence intensity, also plotted in Fig. 13 for comparison. Similar to the fluctuating velocity profile, θ_{rms} is at a maximum very near the wall and decreases moving away. This is only an observation motivated by the long chain of indirect relationships between deflection angles and fluctuating velocity, and more work should be done to obtain a direct or analytical relationship between the two. The scatter in the data in the first 20% of the profile is essentially the error associated with using the model spectrum of Eq. (12).

The θ_{rms} profiles, extracted from the Mag = 4 (green circles and blue diamonds), are consistently below the results from other data sets in the range of $y/\delta < 0.3$. A detailed analysis, performed in [19], revealed that the reason for this discrepancy is the spectral attenuation at the high frequencies due to subaperture effects. These effects lead to lower values of θ_{rms}, compared to Mag = 1.6 and Mag = 1 cases, where the subaperture sizes and the resulting high-end attenuation are smaller.

Figure 17 plots the values of $\mathrm{OPD_{rms}}$ from the same four data sets. While the larger values of the θ_{rms} profile are located closer to the wall, the largest values of $\mathrm{OPD_{rms}}$ resides between $y/\delta = 0.4$–0.8. This means that smaller, near-wall structures contribute most to θ_{rms}, while larger outer structures contribute most to $\mathrm{OPD_{rms}}$. This is consistent with previous findings [3,12]. The factor of f^2 in the denominator of Eq. (9) results in mostly the low end of the spectrum contributing to $\mathrm{OPD_{rms}}$. This means that the same shift in the spectral peak location that was just examined in light of θ_{rms} has the exact opposite effect on $\mathrm{OPD_{rms}}$. Near the wall, the Mag = 4 cases have a larger value of $\mathrm{OPD_{rms}}$ relative to the other magnifications, in some cases by a factor of 1.5.

Assuming that the side-wall boundary layers (BL) have the same thickness as the boundary layer over the development plate, the aerooptical distortions from two side-wall boundary layers can be estimated [3]. The normalized aerooptical distortion from the side-wall boundary layers is also plotted in Fig. 17 as a dashed line. The aerooptical distortions in the spanwise direction are several times larger than the contaminating optical aberrations from side-will boundary layers, justifying the assumption that the contaminating effects can be neglected. The only locations where the contamination might be significant is near the wall, $y/\delta \lesssim 0.1$, and in the freestream outside the boundary layer, $y > \delta$. In these locations, the optical distortions in the spanwise direction should approach zero, as the density fluctuations should be zero at the wall and in the freestream. Instead, the measured results in these regions approach the optical distortions from side-wall boundary layers, labeled by a horizontal dashed line in Fig. 17, indicating a level of contamination from side-wall boundary layers. Assuming that the spanwise and the side-wall optical aberrations are independent, it is possible to remove the side-wall contamination, $\mathrm{OPD_{rms}^{Corrected}} = \sqrt{\mathrm{OPD_{rms}^2} - \mathrm{OPD_{rms,side}^2}}$ [4]. The corrected results are also plotted in Fig. 17 for selected cases as open symbols, further demonstrating that the corrupting effects from the side-wall boundary layers are mostly negligible.

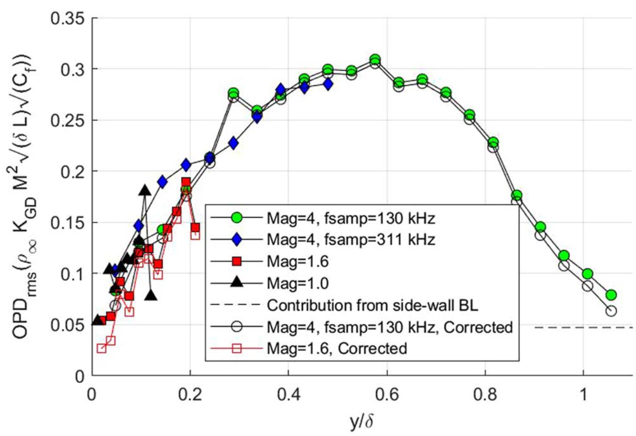

Fig. 17 Normalized $\mathrm{OPD_{rms}}(y)$ profiles for all test cases.

D. Spanwise Density Correlation Length

So far, all the presented results, the convective speeds and aero-optical statistics, were computed directly from the wave front data without any assumptions. The spanwise linking equation, Eq. (6), shows that $\mathrm{OPD_{rms}}$ is proportional to the product of the density fluctuations ρ_{rms} and the spanwise correlation scale $\Lambda_{\rho,z}$. So, if some estimates of the correlation length are given, one can compute the profile of the fluctuating density. This approach was used, for example, to estimate fluctuating density profiles in the nonadiabatic boundary layers [19]. Alternatively, if the fluctuating density profile is known, either through other measurements or numerical simulations, one can compute the spanwise correlation length. In some cases, like for the studied canonical turbulent boundary layer, the strong Reynold's analogy (SRA) can be used to estimate the fluctuating density profile $\rho_{\mathrm{rms}}(y)$ from the velocity statistics $\bar{U}(y)$ and $u_{\mathrm{rms}}(y)$ as [3]

$$\rho_{\mathrm{rms}}(y) = \rho_\infty(\gamma - 1) r M_\infty^2 \left(\frac{\bar{U}(y)}{U_\infty}\right)\left(\frac{u_{\mathrm{rms}}(y)}{u_\tau}\right) \tag{17}$$

where γ is the ratio of specific heats and r is the recovery constant, taken to be 0.89. Using the $\mathrm{OPD_{rms}}(y)$ profiles presented earlier in this chapter and the mean and rms velocity profiles from hot-wire measurements, $\Lambda_{\rho,z}(y)$ can be estimated, using Eq. (6). Figure 18 shows the resulting correlation lengths normalized by the boundary-layer thickness δ. There appears to be a linear trend in the wall-normal direction, indicating that the boundary-layer large-scale structure is proportional to the wall-normal distance, which is consistent with Townsend's attached-eddy hypothesis [33].

The computed correlation length is the characteristic scale of the density fields, and direct measurements of the characteristic scales are very difficult. As an alternative, the SRA can be used to estimate the characteristic scales of the density field from the velocity fields. The basic assumption behind the SRA is that velocity fluctuations and temperature fluctuations are linked. If both the pressure and the total temperature fluctuations are zero, the velocity and temperature fluctuations should be perfectly anticorrelated [44]. In real boundary layers, however, it is not exactly the case, with the normalized cross-correlation function $R_{u'T'} \approx -0.7$ [45]. Nevertheless, the correlation coefficient is still large enough, and temperature and, as a consequence, density fluctuations can be assumed to be approximately proportional to the velocity fluctuations, $u' \approx A\rho'$. In this case, it is straightforward to show that the velocity structure characterized by two-point normalized correlations can be used as an approximation of the density structure,

$$\begin{aligned} R_{uu}(\Delta x) &= \frac{E\{u'(x,y,z,t)u'(x+\Delta x,y,z,t)\}}{u_{\mathrm{rms}}^2} \\ &\approx \frac{E\{A^2\rho'(x,y,z,t)\rho'(x+\Delta x,y,z,t)\}}{A^2\rho_{\mathrm{rms}}^2} \\ &= \frac{E\{\rho'(x,y,z,t)\rho'(x+\Delta x,y,z,t)\}}{\rho_{\mathrm{rms}}^2} = R_{\rho\rho}(\Delta x) \end{aligned}$$

Thus, the SRA suggests that the velocity and density correlation-based lengths are similar. This result will be used in this work to qualitatively compare the results obtained from the spanwise version of the linking Eq. (6) with what is more commonly reported in the literature through two-point velocity correlations.

One difficulty arises from the fact that the integrated correlation velocity length is rarely computed by other researchers. The vast majority use a simple first crossing definition where R_{uu} crosses 0.05. The closest comparison achievable is through extracting spanwise R_{uu} data from the literature and integrating it ourselves. Three R_{uu} plots from Hutchins and Marusic [46] were integrated and included in Fig. 18. This comparison is more of a sanity check than a quantitative comparison because we lack the full data set and R_{uu} was only given for a fixed spanwise extent of $-\delta$ to δ. Also, as discussed previously, the density characteristic length is not necessarily equal to the velocity characteristic length. Considering those issues, the agreement is quite encouraging.

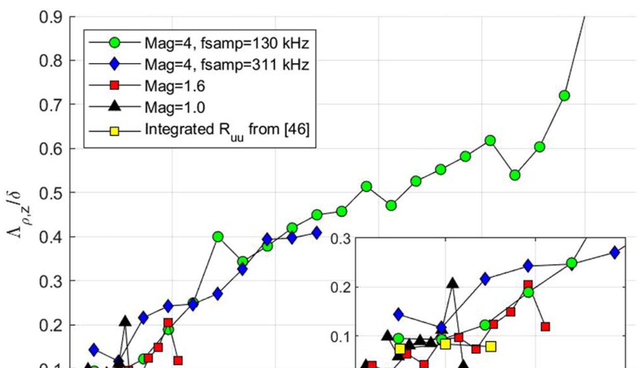

Fig. 18 Spanwise correlation length $\Lambda_{\rho,z}(y)$ computed from the spanwise uniform linking equation, Eq. (6); $\rho_{\mathrm{rms}}(y)$ was computed using Eq. (17). Estimates of $\mathrm{OPD}_{\mathrm{rms}}(y)$ are from Fig. 17. The insert shows zoomed-in results.

V. Conclusions

The work described in this paper is most fundamentally a novel application of an industry standard measurement tool, a Shack–Hartmann wave front sensor. This tool, which had classically been used to measure wall-normal aerooptical distortion in turbulent flows, was applied along the spanwise direction. It was demonstrated that in this case some important fluidic statistics, like the local convective velocities and the spanwise integral scales, can be directly extracted from aerooptical distortions, measured by the wave front sensor. Because of various contaminating effects, specific to the wave front measurements, like subaperture and aperture attenuation effects, several data analysis techniques were revisited in order to correctly compute uncontaminated levels of aerooptical distortions $\mathrm{OPD}_{\mathrm{rms}}$ at different wall-normal locations. The empirical model was used to provide an estimate of the true deflection angle spectra in the presence of contamination at the low end of the spectra. The cleaned-up spectra were used to calculate $\mathrm{OPD}_{\mathrm{rms}}$ as a function of the wall-normal direction. To properly extract the convective speed of the aerooptical structures, two techniques, the spectral cross-correlation method and the dispersion method, were used. It was demonstrated that in cases where the spatial resolution was not sufficiently high the spectral cross-correlation was corrupted by spatial aliasing effects and resulted in biased estimates of the convective speeds. A dispersion analysis, based on the 2-D Fourier transform of optical signal in multiple spatial points, was shown to avoid the aliasing issue. Using the redundancy in temporal/spatial information in multiple spatial points and the nature of discrete 2-D Fourier transform, a new technique, called the stacking method, was proposed. This technique was shown to correctly reconstruct the 2-D spectrum and accurately compute the convective velocity.

A canonical subsonic turbulent boundary layer was used to demonstrate the ability of the optical technique to extract important fluidic parameters, like the velocity profile and the spanwise correlation lengths. Note that the proposed technique can also be implemented to study other spanwise-uniform turbulent flows, like planar shear layers or two-dimensional wakes. Hot-wire measurements were performed to provide the mean velocity statistics in the boundary layer for comparison purposes. In the log region, the optically measured convective velocity was shown to be in good agreement with the mean velocity obtained using a single hot wire. Coupled with the Clauser method, the analysis of the convective velocity in the log-linear region provided an estimate of the skin friction coefficient, which was found to be within 10% of the skin friction coefficient computed from the hot-wire data. The largest shortcoming of optically measured convective velocity was found to be the presence of intermittency effects in the outer region of the boundary layer.

Using the extracted levels of aerooptical distortions and the strong Reynold's analogy, a wall-normal distribution of the spanwise density correlation length was estimated. An approximately linear behavior for the spanwise correlation length with respect to the distance to the wall was observed, consistent with Townsend's attached eddy hypothesis. The values of density correlation length were quantitatively consistent with the velocity correlation lengths, extracted from velocity correlation functions. The extracted density correlation lengths, along with traditional velocity-based correlation lengths, can be used to study the large-scale structure in turbulent boundary layers.

Acknowledgments

This work was supported by the Department of Aerospace and Mechanical Engineering and Laboratory of Flow Physics and Control (FlowPAC) at the University of Notre Dame. The authors would like to acknowledge Matthew Kemnetz, Nicholas De Lucca, and Adam Smith for helping set up the initial optical experiments and for valuable suggestions in reducing the data. The authors would also like to thank Mitchell Lozier for the numerous occasions of help with hot-wire experiments.

References

[1] Wang, M., Mani, A., and Gordeyev, S., "Physics and Computation of Aero-Optics," *Annual Review of Fluid Mechanics*, Vol. 44, No. 1, 2012, pp. 299–321.
https://doi.org/10.1146/annurev-fluid-120710-101152

[2] Jumper, E. J., and Gordeyev, S., "Physics and Measurement of Aero-Optical Effects: Past and Present," *Annual Review of Fluid Mechanics*, Vol. 49, No. 1, 2017, pp. 419–441.
https://doi.org/10.1146/annurev-fluid-010816-060315

[3] Gordeyev, S., Smith, A. E., Cress, J. A., and Jumper, E. J., "Experimental Studies of Aero-Optical Properties of Subsonic Turbulent Boundary Layers," *Journal of Fluid Mechanics*, Vol. 740, 2014, pp. 214–253.
https://doi.org/10.1017/jfm.2013.658

[4] Gordeyev, S., Cress, J. A., Smith, A., and Jumper, E. J., "Aero-Optical Measurements in a Subsonic, Turbulent Boundary Layer with Non-Adiabatic Walls," *Physics of Fluids*, Vol. 27, No. 4, 2015, Paper 045110.
https://doi.org/10.1063/1.4919331

[5] Gordeyev, S., Rennie, M. R., Cain, A. B., and Hayden, T., "Aero-Optical Measurements of High-Mach Supersonic Boundary Layers," *46th AIAA Plasmadynamics and Lasers Conference*, AIAA Paper 2015-3246, 2015.
https://doi.org/10.2514/6.2015-3246

[6] Gordeyev, S., and Juliano, T. J., "Optical Measurements of Transitional Events in a Mach-6 Boundary Layer," *AIAA Journal*, Vol. 55, No. 11, 2017, pp. 3629–3639.
https://doi.org/10.2514/1.J055759

[7] Ferraro, P., Grilli, S., Alfieri, D., Nicola, S. D., Finizio, A., Pierattini, G., Javidi, B., Coppola, G., and Striano, V., "Extended Focused Image in Microscopy by Digital Holography," *Optical Express*, Vol. 13, No. 18, 2005, pp. 6738–6749.
https://doi.org/10.1364/OPEX.13.006738

[8] Parziale, N., Shepherd, J., and Hornung, H., "Differential Interferometric Measurement of Instability in a Hypervelocity Boundary Layer," *AIAA Journal*, Vol. 51, No. 3, 2013, pp. 750–754.
https://doi.org/10.2514/1.J052013

[9] Schmidt, B. E., and Shepherd, J., "Analysis of Focused Laser Differential Interferometry," *Applied Optics*, Vol. 54, No. 28, 2015, pp. 8459–8472.
https://doi.org/10.1364/AO.54.008459

[10] Ceruzzi, A., and Cadou, C. P., "Simultaneous Velocity and Density Gradient Measurements Using Two-Point Focused Laser Differential Interferometry," *AIAA Scitech 2019 Forum*, AIAA Paper 2019-2295, 2019.
https://doi.org/10.2514/6.2019-2295

[11] Butler, L. N., and Gordeyev, S., "Development of the Focused Malley Probe as a Local Aero-Optical Measurement Technique," *AIAA Scitech 2022 Forum*, AIAA Paper 2022-0988, 2022.
https://doi.org/10.2514/6.2022-0988

[12] Jumper, E. J., and Fitzgerald, E. J., "Recent Advances in Aero-Optics," *Progress in Aerospace Sciences*, Vol. 37, No. 3, 2001, pp. 299–339.
https://doi.org/10.1016/S0376-0421(01)00008-2

[13] Gladstone, J. H., and Dale, T. P., "XIV. Researches on the Refraction, Dispersion, and Sensitiveness of Liquids," *Philosophical Transactions of the Royal Society of London*, Vol. 153, Dec. 1863, pp. 317–343.
https://doi.org/10.1098/rstl.1863.0014

[14] Kemnetz, M. R., and Gordeyev, S., "Analysis of Aero-Optical Jitter in Convective Turbulent Flows Using Stitching Method," *AIAA Journal*, Vol. 60, No. 1, 2022, pp. 1–17.
https://doi.org/10.2514/1.J060756

[15] Sutton, G. W., "Effect of Turbulent Fluctuations in an Optically Active Fluid Medium," *AIAA Journal*, Vol. 7, No. 9, 1969, pp. 1737–1743.
https://doi.org/10.2514/3.5384

[16] Hugo, R. J., and Jumper, E. J., "Applicability of the Aero-Optic Linking Equation to a Highly Coherent, Transitional Shear Layer," *Applied Optics*, Vol. 39, No. 24, 2000, pp. 4392–4401.
https://doi.org/10.1364/AO.39.004392

[17] Wang, K., and Wang, M., "Aero-Optics of Subsonic Turbulent Boundary Layers," *Journal of Fluid Mechanics*, Vol. 696, 2012, pp. 122–151.
https://doi.org/10.1017/jfm.2012.11

[18] Wang, K., and Wang, M., "On the Accuracy of Malley Probe Measurements of Aero-Optical Effects: A Numerical Investigation," *Optical Engineering*, Vol. 52, No. 7, 2013, Paper 071407.
https://doi.org/10.1117/1.OE.52.7.071407

[19] Sontag, J., "Optical Characterization of Spanwise Uniform Turbulent Flows," Ph.D. Disseration, Univ. of Notre Dame, Notre Dame, IN, 2021.

[20] Harun, Z., Monty, J. P., Mathis, R., and Marusic, I., "Pressure Gradient Effects on the Large-Scale Structure of Turbulent Boundary Layers," *Journal of Fluid Mechanics*, Vol. 715, 2013, p. 477.
https://doi.org/10.1017/jfm.2012.531

[21] Nightingale, A. M., and Gordeyev, S. V., "Shack-Hartmann Wavefront Sensor Image Analysis: a Comparison of Centroiding Methods and Image-Processing Techniques," *Optical Engineering*, Vol. 52, No. 7, 2013, Paper 071413.
https://doi.org/10.1117/1.OE.52.7.071413

[22] Siegenthaler, J. P., "Guidelines for Adaptive-Optic Correction Based on Aperture Filtration," Ph.D. Dissertation, Univ. of Notre Dame, Notre Dame, IN, 2008.

[23] Smith, A., Gordeyev, S., and Jumper, E., "Aperture Effects on Aero-Optical Distortions Caused by Subsonic Boundary Layers," *43rd AIAA Plasmadynamics and Lasers Conference*, AIAA Paper 2012-2986, 2012.
https://doi.org/10.2514/6.2012-2986

[24] Gordeyev, S., and Jumper, E., "Fluid Dynamics and Aero-Optics of Turrets," *Progress in Aerospace Sciences*, Vol. 46, No. 8, 2010, pp. 388–400.
https://doi.org/10.1016/j.paerosci.2010.06.001

[25] Smith, A. E., Gordeyev, S., Ahmed, H., Ahmed, A., and Wittich, D. J., "Shack-Hartmann Wavefront Measurements of Supersonic Turbulent Boundary Layers in the TGF," *45th AIAA Plasmadynamics and Lasers Conference*, AIAA Paper 2014-2493, 2014.
https://doi.org/10.2514/6.2014-2493

[26] Gordeyev, S., Jumper, E., and Hayden, T. E., "Aero-Optical Effects of Supersonic Boundary Layers," *AIAA Journal*, Vol. 50, No. 3, 2012, pp. 682–690.
https://doi.org/10.2514/1.J051266

[27] Smith, A. E., Gordeyev, S., Saxton-Fox, T., and McKeon, B. J., "Subsonic Boundary-Layer Wavefront Spectra for a Range of Reynolds Numbers," *45th AIAA Plasmadynamics and Lasers Conference*, AIAA Paper 2014-2491, 2014.
https://doi.org/10.2514/6.2014-2491

[28] Gordeyev, S., Hayden, T. E., and Jumper, E. J., "Aero-Optical and Flow Measurements over a Flat-Windowed Turret," *AIAA Journal*, Vol. 45, No. 2, 2007, pp. 347–357.
https://doi.org/10.2514/1.24468

[29] Gordeyev, S., and Kalensky, M., "Effects of Engine Acoustic Waves on Aerooptical Environment in Subsonic Flight," *AIAA Journal*, Vol. 58, No. 12, 2020, pp. 5306–5317.
https://doi.org/10.2514/1.J059484

[30] Del Álamo, J. C., and Jiménez, J., "Estimation of Turbulent Convection Velocities and Corrections to Taylor's Approximation," *Journal of Fluid Mechanics*, Vol. 640, 2009, pp. 5–26.
https://doi.org/10.1017/S0022112009991029

[31] Lynch, K. P., Spillers, R., Miller, N. E., Guildenbecher, D., and Gordeyev, S., "Aero-Optical Measurements of a Mach 8 Boundary Layer," *AIAA Aviation 2021 Forum*, AIAA Paper 2021-2831, 2021.
https://doi.org/10.2514/6.2021-2831

[32] Clauser, F. H., "The Turbulent Boundary Layer," *Advances in Applied Mechanics*, Vol. 4, Elsevier, New York, 1956, pp. 1–51.
https://doi.org/10.1016/S0065-2156(08)70370-3

[33] Townsend, A. A., *The Structure of Turbulent Shear Flow*, Cambridge Univ. Press, Cambridge, England, U.K., 1980, pp. 262–263.
https://doi.org/10.1017/S0022112056210366

[34] Nagib, H. M., and Chauhan, K. A., "Variations of von Kármán Coefficient in Canonical Flows," *Physics of Fluids*, Vol. 20, No. 10, 2008, p. 101518.
https://doi.org/10.1063/1.3006423

[35] Österlund, J. M., "Experimental Studies of Zero Pressure-Gradient Turbulent Boundary Layer Flow," Ph.D. Dissertation, Mekanik, Stockholm, Sweden, 1999.

[36] Nagib, H., Christophorou, C., Ruedi, J.-D., Monkewitz, P., Osterlund, J., Gravante, S., Chauhan, K., and Pelivan, I., "Can We Ever Rely on Results from Wall-Bounded Turbulent Flows Without Direct Measurements of Wall Shear Stress?" *24th AIAA Aerodynamic Measurement Technology and Ground Testing Conference*, AIAA Paper 2004-2392, 2004.
https://doi.org/10.2514/6.2004-2392

[37] Wei, T., Schmidt, R., and McMurtry, P., "Comment on the Clauser Chart Method for Determining the Friction Velocity," *Experiments in Fluids*, Vol. 38, No. 5, 2005, pp. 695–699.
https://doi.org/10.1007/s00348-005-0934-3

[38] Hutchins, N., Nickels, T. B., Marusic, I., and Chong, M., "Hot-Wire Spatial Resolution Issues in Wall-Bounded Turbulence," *Journal of Fluid Mechanics*, Vol. 635, 2009, p. 103.
https://doi.org/10.1017/S0022112009007721

[39] Geng, C., He, G., Wang, Y., Xu, C., Lozano-Durán, A., and Wallace, J. M., "Taylor's Hypothesis in Turbulent Channel Flow Considered

Using a Transport Equation Analysis," *Physics of Fluids*, Vol. 27, No. 2, 2015, Paper 025111.
https://doi.org/10.1063/1.4908070

[40] Liu, C., and Gayme, D. F., "An Input-Output Based Analysis of Convective Velocities in Turbulent Channels," *Journal of Fluid Mechanics*, Vol. 888, April 2020, p. A32.
https://doi.org/10.1017/jfm.2020.48

[41] Del Alamo, J. C., and Jiménez, J., "Spectra of the Very Large Anisotropic Scales in Turbulent Channels," *Physics of Fluids*, Vol. 15, No. 6, 2003, pp. L41–L44.
https://doi.org/10.1063/1.1570830.

[42] LeHew, J., Guala, M., and McKeon, B., "A Study of the Three-Dimensional Spectral Energy Distribution in a Zero Pressure Gradient Turbulent Boundary Layer," *Experiments in Fluids*, Vol. 51, No. 4, 2011, pp. 997–1012.
https://doi.org/10.1007/s00348-011-1117-z

[43] Hutchins, N., and Marusic, I., "Large-Scale Influences in Near-Wall Turbulence," *Philosophical Transactions of the Royal Society A: Mathematical, Physical and Engineering Sciences*, Vol. 365, No. 1852, 2007, pp. 647–664.
https://doi.org/10.1098/rsta.2006.1942.

[44] Smits, J. A., and Dussauge, J. P., *Turbulent Shear Layers in Supersonic Flow*, 2nd ed., Springer-Verlag, New York, 2006, pp. 127–130.
https://doi.org/10.1007/b137383

[45] Priebe, S., Wu, M., and Martín, M. P., "Direct Numerical Simulation of a Reflected-Shock-Wave/Turbulent-Boundary-Layer Interaction," *AIAA Journal*, Vol. 47, No. 5, 2009, pp. 1173–1185.
https://doi.org/10.2514/1.38821

[46] Hutchins, N., and Marusic, I., "Evidence of Very Long Meandering Features in the Logarithmic Region of Turbulent Boundary Layers," *Journal of Fluid Mechanics*, Vol. 579, May 2007, pp. 1–25.
https://doi.org/10.1017/S0022112006003946

C. Lee
Associate Editor